Simulation of a soft-gamma-ray polarimeter on board a microsatellite[*]

Xiang-Man Liu,[1,2,3] Shu-Wen Tang,[1,2,†] Wei Wang,[4,5,‡] Yu-Hong Yu,[1,2] Zhi-Yu Sun,[1,2] Yong-Jie Zhang,[1,2] Fang Fang,[1,2] Duo Yan,[1,2] Shi-Tao Wang,[1,2] Xue-Heng Zhang,[1,2] Shu-Ya Jin,[1,2] and Bi-Tao Hu[3]

[1]*Institute of Modern Physics, Chinese Academy of Sciences, Lanzhou 730000, China*
[2]*School of Nuclear Science and Technology, University of Chinese Academy of Sciences, Beijing 100049, China*
[3]*School of Nuclear Science and Technology, Lanzhou University, Lanzhou 730000, China*
[4]*Department of Astronomy, School of Physics and Technology, Wuhan University, Wuhan 430072, China*
[5]*Wuhan University-National Astronomical Observatories Joint Center for Astronomy, Wuhan University, Wuhan 430072, China*

Gamma-ray polarimetry is a new and prospective tool for studying various extreme high-energy celestial objects and is of great significance for the development of astrophysics. With the rapid development of microsatellite technology, the advantages in space exploration are becoming increasingly apparent. Therefore, in this paper, we conducted a simulation study on a soft gamma-ray polarimeter for a microsatellite in space. Here, we proposed a unique design structure for the polarimeter based on the microsatellite design concept and the Compton scattering principle. And then, the detailed Monte Carlo simulations using mono-energetic gamma-ray linear polarization sources and the Crab-like sources in the energy range of 0.1-10 MeV with full consideration of the orbital background were performed. The simulation results show that the polarimeter can exhibit excellent polarization detection performance. The modulation factor is 0.80±0.01, and the polarization angles are accurate within an error of 0.2° at 200 keV for on-axis incidence. For the Crab-like sources for on-axis incidence, the polarization degrees are consistent with the set values within the error tolerance, the modulation factor is 0.76±0.01, and the minimum detectable polarization reaches 2.4% at 3σ for an observation time of 10^6 seconds. In addition, the polarimeter has recoil electron tracking, imaging, and powerful background suppression at a large field of view ($\sim 2\pi$ sr). The polarimeter designed can meet the requirements of a space-soft gamma-ray polarization detector very well and has a bright research prospect.

Keywords: Soft Gamma-ray, Polarization, Compton scattering, Microsatellite, Monte Carlo simulation

I. INTRODUCTION

Gamma-ray polarization measurement in gamma-ray astronomy is broadly considered to be a new and powerful diagnostic tool for some critical open questions or doubts about the most extreme high-energy sources: gamma-ray bursts (GRBs), pulsars, active galactic nuclei (AGNs), binary black holes (BBHs), etc. [1, 2], and these questions or doubts might not be resolved or explained through the timing, energy, and direction of gamma rays. For GRBs studies, polarization measurements can illuminate the nature of the central engines that produce ultra-relativistic jets in GRBs, as well as the physical properties, the radiation mechanisms, and the energy dissipation points of these jets, and can also contribute to the constraints of the theoretical models of the origin of GRBs [1, 3–6]. Detecting gamma-ray polarization emitted by pulsars can help estimate the magnetic field structure around compact objects, to understand the mechanism of gamma-ray emission (curvature radiation or synchrotron radiation), and to speculate on particle acceleration and pair-cascading processes in the magnetosphere of pulsars [1, 7]. In particular, accreting black hole (BH) systems, including BBHs and AGNs, are considered to radiate linearly polarized X-rays and gamma rays owing to scattering processes in their accretion disks, and therefore, the measurement of these polarization features will allow us to identify the geometry of the corona [2, 8]. Many more examples of space gamma-ray polarization as a unique tool to study high-energy astrophysics can be found in Ref. [9–13]. In conclusion, gamma-ray polarization is uniquely helpful and valuable for astrophysical studies as an up-and-coming tool, which makes space gamma-ray polarization measurements extremely attractive.

Under the tremendous scientific lure of space gamma-ray polarization, many astrophysicists from various countries have joined the team to detect space gamma-ray polarization and have made efforts in polarization detection by launching satellites and flying high-altitude balloons. A few typical polarization-related satellite experiments are an X-ray polarimeter onboard the eighth Orbiting Solar Observatory (OSO-8) mission [14], the Ramaty high energy solar spectroscopic imager (RHESSI) mission [15], IBIS and SPI onboard International Gamma-ray astrophysics laboratory (INTEGRAL) [12, 16], GAP onboard IKAROS spacecraft [17], POLAR placed on the Chinese space station TG-2 [18], and cadmium zinc telluride imager (CZTI) onboard ASTROSAT satellite [19]. In addition to the satellite experiments mentioned above, there are several representative balloon experiments: the Polarimeter for High ENErgy X-rays (PHENEX) [20], the Polarised Gamma Ray Observer (PoGO) [21], PoGO+ [22], the Gamma RAy Polarimeter Experiment (GRAPE) [23], the Gamma-Ray Astro-Imager with Nuclear Emulsion (GRAINE) experiment [24]. Although the number of polarization detection experiments available is relatively large (as listed above), most are focused on the X-ray band, especially the hard X-ray band (tens to hundreds of keV), with a few detecting high-energy (>~10 MeV)

gamma-ray polarization, and an extreme lack for the soft gamma-ray band ($\sim$0.1-10 MeV), specifically above 1 MeV.

Generally, the most efficient way to detect the polarization of soft gamma rays is based on the Compton scattering principle. This is because the radiation physics processes occurring in soft gamma rays with matter are dominated by Compton scattering, similar to detecting low- and high-energy gamma-ray polarization dominated by the photoelectric effect and the electron-positron pair production, respectively. Here, it is worth noting that the Medium Energy Gamma-Ray Astronomy (MEGA) telescope [25], based on the Compton scattering principle, has been shown in ground tests to be capable of detecting soft gamma-ray polarization. Unfortunately, the MEGA project was not completed for various reasons. In addition, the Compton Spectrometer and Imager (COSI) [26], also based on the Compton scattering principle, is equally sensitive to gamma-ray polarization in this energy band. However, COSI is only an end-of-flight balloon experiment and faces many challenges in gamma-ray polarization detection as a balloon payload. The most important of these challenges are atmospheric absorption and scattering, and limited exposure. This significantly reduces the ability of the detector to detect soft gamma-ray polarization in space. The best solution to the above problem is to send the detector into space, namely by launching a detection satellite. Given the above analysis, there is a great need to propose and implement a satellite project on soft gamma-ray polarimetry in space to occupy this almost empty energy region, which is of great scientific importance for astrophysical research.

There is no doubt that the best way to measure gamma-ray polarization in the universe is to launch detection satellites. What needs to be highly concerned in recent years is that with the development of science and technology, the development of modern small satellites has become more and more rapid and has significant advantages: small size, lightweight, high technology, short development cycle, low cost, can be standardized stars and modular design technology, can be mass production and storage in the flow line and easy to launch [27, 28]. However, compared with modern small satellites, traditional exploration satellites have apparent disadvantages such as large size and weight, complex technology, long development period, high cost, high risk, and difficulty in achieving [27, 28]. Given this, modern small satellites can give a new perspective to cosmic gamma-ray polarimetry.

To achieve a high-precision and all-sky survey of the polarization of soft gamma rays in space, the idea of using a constellation composed of multiple microsatellites is promising, like the "GRID mission" [29]. Apparently, excellent polarization detection performance is essential for each of the microsatellites in the constellation. Therefore, in this paper, a detailed study was carried out for a microsatellite (polarimeter): a novel detector design based on the principle of Compton scattering was proposed to detect the linear polarization of soft gamma rays, a detector mass model used for simulation was constructed, and a detailed simulation experiment using Monte Carlo methods was implemented to verify its performance. The simulation results showed that the polarimeter designed has excellent performance. Overall, this work validates the rationality of our proposed detector design scheme, lays a solid foundation for future polarimeter development, and offers a meaningful reference for other researchers to design and develop detection satellites.

II. PRINCIPLES AND METHODS

A. Principle of polarization measurement

In the soft gamma-ray domain, the Compton scattering effect becomes a dominating process in interactions of photons with matter. Compton scattering preserves the polarization information of linearly polarized photons to a certain degree. Expressly, when linearly polarized photons and matter undergo Compton scattering, the azimuthal angle distribution of the scattered photon is related to the polarization degree and direction of the incident photon. Therefore, the soft gamma-ray polarimeter in this paper is based on this principle to detect the gamma-ray polarization signals in the universe.

If the initial gamma ray is linearly polarized, then its Compton scattering process can be graphically demonstrated in Fig. 1. Additionally, the Compton scattering differential cross-section of the linearly polarized photon can be expressed by the Klein-Nishina formula as [18]

$$
\begin{aligned}
\frac{d\sigma}{d\Omega} &= \frac{r_0^2}{2}\left(\frac{E'}{E}\right)^2\left(\frac{E}{E'} + \frac{E'}{E} - 2\sin^2\theta\cos^2\eta\right) \\
&= \frac{r_0^2}{2}\left(\frac{E'}{E}\right)^2 \\
&\quad \left\{\frac{E}{E'} + \frac{E'}{E} - \sin^2\theta + \sin^2\theta\cos\left[2\left(\eta+\frac{\pi}{2}\right)\right]\right\},
\end{aligned}
\tag{1}
$$

where r_0 is the classical electron radius, E is the incident or initial photon energy, E' is the scattered photon energy, θ is the Compton scattering angle, and η is the angle between the scattering direction of the scattered photon and the polarization direction of the incident photon (i.e., the azimuthal angle) shown in Fig. 1. E'/E in Eq. (1) can be represented by the Compton equation [1]

$$
\frac{E'}{E} = \left[1 + \frac{E}{m_e c^2}(1-\cos\theta)\right]^{-1},
\tag{2}
$$

where $m_e c^2$ is the electron rest mass energy. It can be seen from Eq. (1) that linearly polarized photons tend to scatter perpendicularly to the incident polarization vector (minimizing the term $2\sin^2\theta\cos^2\eta$). In addition, when both E'/E and θ are constants, the differential scattering cross-section of polarized photons will obey the $cos[2(\eta + \pi/2)]$ distribution, namely, the variation of the number of scattered photons with the azimuthal angle η obeys the cosine distribution. In practice, the incident photon energy E and the scattering angle θ are often non-constant but take on a range of values, and what we actually measure is the averaging effect, but this does not affect the fact that the averaged azimuth follows a cosine distribution.
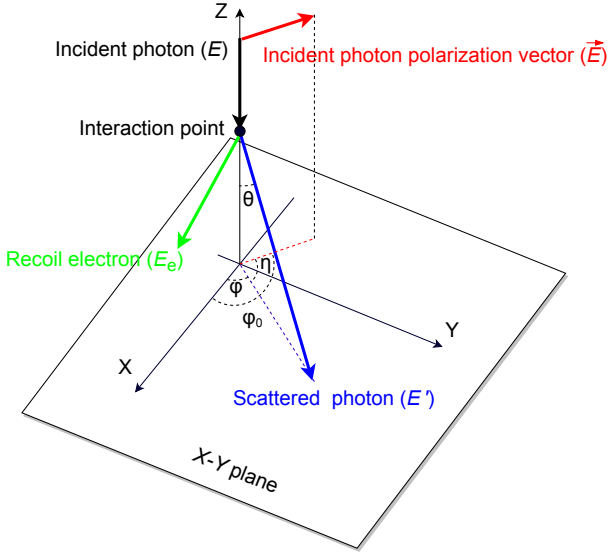
Fig. 1. (Color online) The schematic of Compton scattering of a linearly polarized photon.

In most cases, since η cannot be measured directly, the polarization information of incident linearly polarized photons cannot be obtained using the method of measuring η. Given the above practical situation, the angle φ is introduced as the Compton scattering azimuth, which is the angle between the polarized scattered photon plane and the X-axis, as shown in Fig. 1. Polarization signatures of a source of incident linearly polarized photons are reflected in the distribution of the azimuthal angle φ that can be described by the following function

$$f(\varphi) = A \left\{ 1 + \mu \cos \left[2 \left(\varphi - \varphi_0 \right) + \pi \right] \right\}, \qquad (3)$$

which can be easily deduced from Eq. (1). Here, φ_0 represents the polarization angle of the incident photon or the direction of the original polarization vector (see Fig. 1), A is the offset of the distribution of the azimuthal scatter angle (see Fig. 2), and μ is a significant parameter called modulation factor which can describe the polarization response of a polarimeter. Equation (3) can be shown graphically in Fig. 2, and the curve in Fig. 2 is called the modulation curve. The modulation factor μ can be expressed by the equation

$$\mu = \frac{F_{\max} - F_{\min}}{F_{\max} + F_{\min}} = \frac{B}{A} = \frac{\sin^2 \theta}{\frac{E'}{E} + \frac{E}{E'} - \sin^2 \theta}, \qquad (4)$$

which can be derived from Eqs. (1), (2), and (3), where F_{max}, F_{min}, A, and B are represented in Fig. 2. For a fully (100%) linearly polarized photon beam, the modulation factor is expressed as μ_{100}, while for a photon beam with an unknown polarization degree, the modulation factor is μ. The polarization degree of the incident photons can be obtained by the equation

$$P = \frac{\mu}{\mu_{100}}, \qquad (5)$$

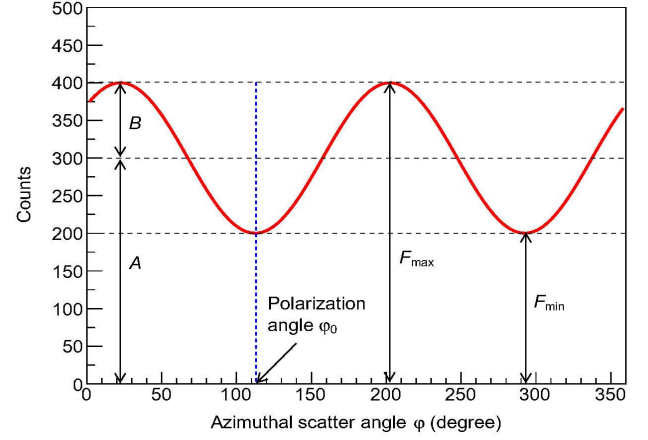where P is a positive value between 0 and 1.

Fig. 2. (Color online) The distribution of the azimuthal scatter angle φ.

Figure 3 illustrates the relationship (the functional relationship expressed in Eq. (4)) among the modulation factor μ_{100}, a key performance parameter of a polarimeter, the Compton scatter angle θ and the incident photon energy E. It can be intuitively seen from Fig. 3 that the modulation of the azimuthal distribution is most significant at lower energies and medium scattering angles. For photons with extremely large ($\theta \approx 180°$) or small ($\theta \approx 0°$) scattering angles, they carry little polarization information. Additionally, we can also see that the modulation factor μ_{100} decreases significantly with the increase of photons energy.
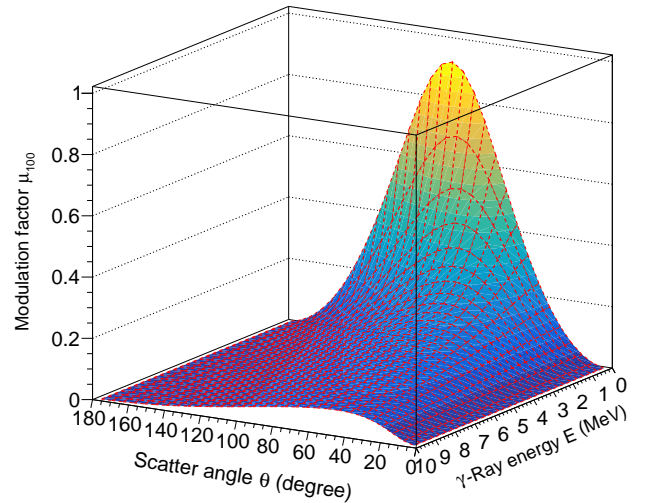

Fig. 3. (Color online) The modulation factor μ_{100} as a function of the Compton scatter angle θ and the incident photon energy E.

Besides the modulation factor, the minimum detectable polarization (MDP) (also known as polarization sensitivity, i.e., the detection limit of the degree of polarization [30]) is also an

essential performance parameter to describe the performance of a polarimeter. The MDP is used to judge the polarization detection capability of a polarimeter, which can be calculated as follows [1]

$$MDP = \frac{n_\sigma}{\mu_{100}S} \sqrt{\frac{S+B}{T}}, \qquad (6)$$

where n_σ is related to the expected confidence level of the detection (e.g., $n_\sigma = 3$), and S and B are the count rates of the source and background (after all event selection cuts are applied) in the observation time T, respectively. As can be seen from Eq. (6), the MDP is related to five parameters. In general, n_σ, μ_{100}, and T are all constants once the confidence level, the polarimeter, and the observation time have been determined. Then the MDP is only affected by S and B, and the MDP gets better with increasing S and worse with increasing B. Considering that the angular resolution will be used as the key event selection condition when calculating S and B, S and B are then related to the angular resolution of the detector. In fact, the excellence of angular resolution has almost no effect on S, while it has a significant effect on B. When the angular resolution is excellent, B becomes smaller, resulting in a better MDP for the polarimeter. In contrast, when the an-

gular resolution is poor, B becomes larger, leading to a worse MDP for the polarimeter. From the above analysis, it can be seen that the angular resolution significantly affects the polarization sensitivity of a polarimeter, which will be a valuable guide to the design of a polarimeter.

B. Polarimeter design

In this paper, the polarimeter was designed to detect the polarization information of linearly polarized gamma rays in the energy range of 0.1-10 MeV based on the Compton scattering principle. The structure design of our proposed polarimeter is shown in Fig. 4, where the whole model contains only active materials. As a whole, the polarimeter is mainly made up of three detection sub-systems: a silicon converter (blue) located in the upper center of the polarimeter, a CsI absorber (red) surrounding the converter on five sides (except the top side), and an organic plastic scintillator anticoincidence shield (ACS) (green) which envelops the two sub-detectors mentioned above. The whole detector containing only sensitive material has a size of $26\times26\times20$ cm^3 and a mass of ~15 kg. The design details and description of each sub-detector of the polarimeter are given in the following.

TABLE 1: Design parameters of each sub-detector in the polarimeter.

Sub-detectors	Design shape	Sensitive materials	Total mass (kg)	Cell size (cm^3)	Number of cells	Photon absorption probability @ 1MeV (%)	Layer spacing (cm)	Number of strips on a cell and strip pitch
Converter	Multi-layer array	Silicon	~0.2	$10\times10\times0.1$	10	~15	0.5	50, 2mm
Absorber	Pixel-type array	CsI	~11.5	Bar:$1\times1\times6$ Cube:$2\times2\times2$	Bar:256 Cube:128	Bar:~80 Cube:~42	-	-
ACS	Hollow shell	Organic plastic scintillator	~3.3	$26\times26\times20$, thickness:1cm	1	-	-	-

Converter The converter plays a vital role in the polarimeter. It performs two main tasks: first, the first Compton interaction takes place in the converter, and second, the converter records the deposited energy and the interaction position of all generated particles. To accomplish the above tasks, the converter is required to enable photons to have a high Compton scattering probability in it, to be able to stop recoil electrons, and to have better energy and position resolution. After comprehensive consideration, it was agreed that a multi-layer double-sided silicon strip detector was the best converter design choice. Silicon, a low-Z material, has a higher Compton cross-section than medium-Z and high-Z materials such as Ge and CdZnTe in the 0.1 to 10 MeV energy range. The double-sided silicon strip detector has a low threshold and guarantees excellent energy and two-dimensional (i.e., X and Y direction) position resolution. Furthermore, multiple thin-layer configurations can enlarge Compton scattering cross section, provide longitudinal position information, and track and absorb recoil electron energy
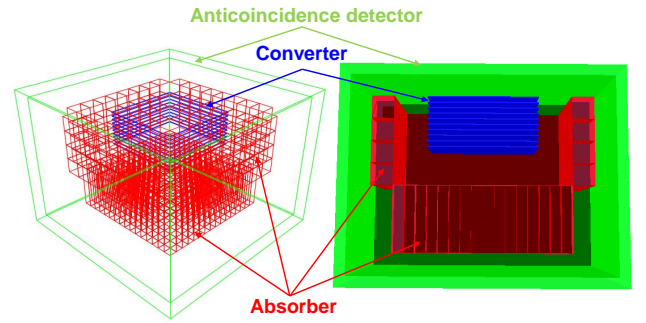

Fig. 4. (Color online) The wireframe model (Left) and the mass model (Right) of the polarimeter, which consists of the outer organic plastic scintillator anticoincidence shield (green), a silicon converter (blue) located in the upper middle, and a CsI absorber (red) surrounding the five sides of the converter.

as much as possible. The overall geometric model of the converter and its physical location in the overall system can be

seen in blue in Fig. 4, and the detailed design parameters are given in Table 1.

Absorber The absorber (also known as a calorimeter) is required to stop scattered Compton photons and measure their energy and position information. Additionally, since the Compton scattering polarization signature is particularly significant at larger scattering angles and lower energies, the absorber must be able to measure large-angle scattered photons. Finally, the absorber is expected to act as a barrier to reduce the radiation from the space orbit environment to the converter and improve the background rejection of the entire detector. Therefore, an absorber that meets the requirements needs to use high-Z materials as the detection medium, has good energy and position resolution, has a large acceptance of scattered photons, and can surround the converter as much as possible. The CsI scintillator is the better choice as the sensitive material of the absorber because of its high density, large atomic number, high light yield, good mechanical properties, not easy to deliquescence, high detection efficiency, ease of processing into small pixels of various shapes, availability in large quantities, and reasonable price [31]. A pixel-type absorber composed of CsI crystals was the solution we finally chose. Two types of crystal cells were used: cubic crystals and bar crystals. The overall geometric configuration of the absorber and its physical position in the overall system is given by the red part in Fig. 4, and some design parameters can be found in Table 1. Considering the power consumption and space constraints of a compact microsatellite, silicon photomultipliers (SiPMs) were planned to be used as photoelectric converters for CsI crystals instead of traditional photomultiplier tubes (PMTs) owing to their attractive abilities, such as their super miniature size, low power consumption, low weight, small size, fast time response, large self-gain (10^5-10^6), high signal-to-noise ratio and insensitivity to magnetic fields [29, 32]. Each small cubic crystal was expected to couple the photoelectric converter only on the side facing away from the silicon converter to minimize the passive material between the converter and absorber. For bar crystals, a dual-ended readout scheme will be used. To verify the feasibility of the scheme, we have done a detailed test study for the CsI detection cell in the laboratory, the details of which can be read in Refs. [31, 33]. The experimental results have shown that the CsI detection cell exhibits good performance, the energy resolution is close to 5% (full width at half maximum, FWHM), and the longitudinal position resolution is approximately 5 mm (FWHM) for 662 keV gamma-ray emitted by the ^{137}Cs source. The method of the dual-ended readout can not only ensure better energy resolution but also give the position information along the crystal bar direction (Z-direction).

ACS The ACS of the polarimeter is mainly to veto background events induced primarily by charged particles (e.g., protons, alphas, electrons, and positrons) from the orbital environment in space (described in Sec. II D). A shell-shaped hollow plastic scintillator with a thickness of 1 cm was used as an anticoincidence shield to completely cover the converter and the absorber. The green part in Fig. 4 shows the geometric configuration of the ACS and its physical location in the overall system. Meanwhile, some design parameters are given in Table 1.

C. Simulation and analysis tools

The Medium Energy Gamma-ray Astronomy library (MEGAlib) [34] is an open-source Monte Carlo simulation and data analysis package wholly written in C++ and based on ROOT [35] and Geant4 [36]. It was explicitly designed for gamma-ray detectors in the low-to-medium energy region. It could be used for the design of the detector geometry and the simulation of the interaction process of gamma rays and other particles with matter, as well as data analysis. The reliability of the MEGAlib package for the simulation and data analysis of low- and medium-energy gamma-ray detectors has been recognized by researchers in this specialized field. To date, MEGAlib has been successfully applied to various hard X-ray/gamma-ray telescope projects and studies in space and on the ground, such as MEGA [37], COSI [26], AMEGO [38], COMPTEL [39], ACT [40], TIGRE [41], e-ASTROGAM [7], a combined Compton and coded-aperture telescope for medium-energy gamma-ray astrophysics [42], and many more.

The simulation of a detector based on MEGAlib first requires the creation of a realistic geometry by using the Geomega package contained in MEGAlib [34, 37, 41], as shown in Fig. 4. The geometry includes the shape, size, location, material, and properties of the surrounding environment for each volume that makes up the detector. The cosmic simulator, Cosima, integrated with the MEGAlib package, is used to perform Monte Carlo simulations [34, 37, 41]. Cosima can combine Geant4 and the specified source to simulate particle transport and interaction with geometric materials and then generate an output file that stores the simulated interaction information. The simulation data analysis is performed using Revan and Mimrec contained in MEGAlib [34, 37, 41, 43]. Then, we can get the simulation results. In addition, MEGAlib needs to use the background data computed and generated by the LEOBackground software package [44], written entirely in Python, to simulate the low-earth orbit (LEO) environment. The above is only a brief overview of the functions of the main sub-packages of MEGAlib; a detailed description and usage can be found in Ref. [34, 37, 41, 43, 44].

D. Simulation method

Currently, simulation experiments are the primary method we use to study the performance of our designed polarimeter. In this section, the simulation method of the polarimeter is illustrated, including an overview of the simulation experiment flow, the detailed configuration of the performance parameters of each sub-detector, the configuration of the particle sources (gamma-ray sources and background sources), and a brief data analysis process.

Figure 5 shows a brief flow of our simulation experiments using the MEGAlib package. First, a realistic geometric

model of the detector was constructed, while reasonable performance parameters were set for the detector in order to adapt the simulation to reality. In addition, gamma rays and background sources were similarly configured. It should be mentioned that the configuration of particle sources also involved setting information such as the physics list, data output formats, data storage files, simulation stop conditions, etc. Next, Geant4 would be called by MEGAlib to complete the Monte Carlo simulation. The simulated data were then reconstructed (i.e., Compton event reconstruction) using the proven event reconstruction algorithm in MEGAlib. Finally, the simulation results were obtained after a high-level analysis of the reconstructed events using MEGAlib. A brief description of the simulation process has been given above, and a more detailed elaboration will be shown in the following.

verter were assumed to have a uniform energy resolution of 10 keV FWHM as well as a noise threshold of 15 keV and a trigger threshold of 30 keV [37]. The position resolution of the converter was determined by the number of strips and the thickness of each silicon wafer (described in Sec. II B). For the CsI absorber, energy resolutions of 15% FWHM at 100 keV, 9% FWHM at 350 keV, 6.5% FWHM at 511 keV, 5% FWHM at 662 keV, 3.5% FWHM at 1000 keV and 2.7% FWHM at 5000 keV, a noise threshold of 30 keV, and a trigger threshold of 50 keV were set [31, 33, 37]. The depth resolution (Z-direction) of the 6 cm CsI crystal was assumed to be 0.5 cm FWHM [31, 33], but no depth resolution was given for the 2 cm cubic crystal. In addition, the geometry of crystals will determine their spatial resolution, the specific parameters of which can be seen in Sec. II B of the paper. The organic plastic scintillator ACS used an energy resolution of 10 keV (1σ Gaussian), a trigger threshold of 100 keV, and a detection efficiency of 99.9% for charged particles.

Since the MEGAlib package provides the function of user-defined particle sources, we can flexibly set the particle sources for the simulation according to our needs. For our purposes, we have used monochromatic, negative power law, and the file format (generated by the LEOBackground software package) for the energy spectrum, as well as beam parameters for the far-field point source (i.e., homogeneous beam) and the far-field area source. When setting up particle sources, we also took into account the fact that far-field sources are so far away and that they arrive at the detector in the form of plane waves. In our simulation experiments, a total of three types of sources were applied to the three simulations. First, a monochromatic homogeneous beam with a flux of 1.0 ph/cm^2/s was simulated and used to irradiate the mass model of the polarimeter. The polarization response of the polarimeter was studied by varying the energy, angle, and polarization direction of incident photons. Next, the homogeneous beam was repeated with a power law energy spectrum to simulate a discrete celestial source of linearly polarized gamma rays (i.e., a Crab-like source). For the Crab-like source, events were generated by linearly polarized and unpolarized photon beams with an energy spectrum of $4\times10^{-3}E^{-2}$ ph/cm^2/s/MeV between 0.1 and 10 MeV [45]. A simulation experiment was performed using this type of source to investigate the polarization response of the polarimeter to realistically polarized photons and its polarization performance. Third, an isotropic beam source (i.e., a far-field area source) with a spectrum in file form was constructed. In fact, this type of source was used to simulate the space orbit environment. Since the polarimeter is expected to complete a satellite mission, it is quite necessary to consider the impact of the complex space orbit environment on the detector. The background environment depends to a large extent on the orbit in which the satellite is operating. In this case, a typical LEO with an altitude of 550 km and a 0° inclination was selected. The detection of the corresponding orbital background environments by the Beppo-SAX [46] and AGILE [47] missions has made orbital background environments like this one well-known. Figure 6 shows the background environment used in the polarimeter simulation ex-

Fig. 5. (Color online) A brief flow of simulation experiments using MEGAlib.

As a realistic geometric model of the polarimeter constructed using the MEGAlib package has been shown in Fig. 4 and described in detail in Sec. II B, it will not be repeated here. However, it is essential to elaborate on the performance parameter settings of the detector. To make the simulation results reflect the actual situation of the detector as much as possible, the setting of simulation parameters is crucial, which means that reasonable parameters can make the performance of the detector obtained by the simulation experiment closer to that of the real detector and more reliable. The double-sided silicon strip detectors that made up the con-

periments, calculated and given by LEOBackground. As can be seen in Fig. 6, the background components consist of cosmic and albedo photons, hadrons (e.g., neutrons, protons, and alphas), and leptons (e.g., electrons and positrons). It is worth mentioning that the energy spectra in file form that we used for the simulation experiments are exactly these background energy spectra.
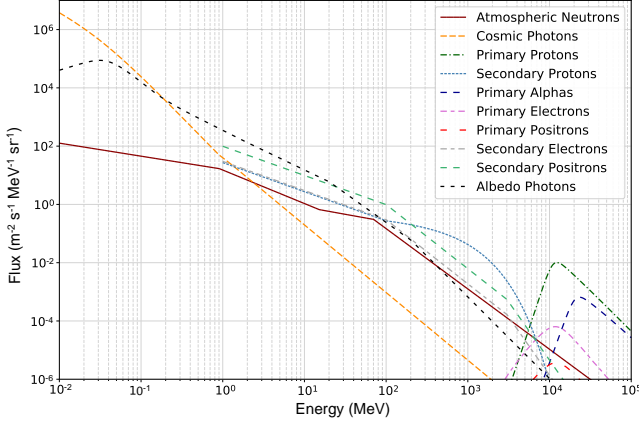

Fig. 6. (Color online) The background environment of the polarimeter on an orbit with an altitude of 550 km and a 0° inclination.

For data analysis, first, a coincident event filter was adopted to select events that satisfy at least one hit in the converter as well as at least one hit in the absorber. Next, the Compton sequence reconstruction (CSR) algorithm with trajectory tracking [37] was applied to these selected events for Compton event reconstruction, which would require that the first hit in the event needs to occur in the converter. Then the information related to the incident photon could be obtained, such as the initial energy, the incident direction, and the scattering angle of the incident photon. All of the above was done by Revan contained in MEGAlib, where the event selection method ensures the integrity of Compton events and plays a vital role in reducing background events. Finally, the reconstructed events would be further processed and analyzed by the Mimrec tool in MEGAlib, including event cuts, plotting of the reconstructed energy spectrum, the evaluation of the angular resolution measurement (ARM) specified as the angular distance between a known source position and the closest reconstructed position on the Compton cone, calculation and correction of modulation curves, image reconstruction, etc. When we analyzed the reconstructed events, we adopted the same and fixed event cuts for events generated by monoenergetic photons, including a $\pm 3\sigma$ photopeak energy window and a $\pm 3\sigma$ ARM cut. In addition, there was a variable event cut, namely the scattering angle cut, which would be adjusted according to the different photon energies, and the scattering angle window is roughly chosen between 40° and 110°. For events generated by Crab-like sources, both a $\pm 3\sigma$ ARM window and a [60°, 110°] Compton scattering angle window were applied as event cuts, and no energy cut was used. Similarly, for events generated by the background sources in the polarimeter, the same event analysis method was used. After the above data processing series, the distribution of azimuthal scattering angles was obtained. Then, the polarization information of the incident photons would be gained from the parameters fitted to the azimuthal distribution.

III. RESULTS AND DISCUSSION

In simulated experiments, various radiation physics processes occur when soft gamma rays are incident in the polarimeter. These physical processes are mainly photoelectric effect, Compton scattering (see γ_1 and γ_2 in Fig. 7), and electron-positron pair creation, with Compton scattering dominating. Of course, gamma rays will also not interact with matter at all, such as γ_3, γ_4, and γ_5 in Fig. 7. As the polarimeter designed in this paper is based on the Compton scattering principle for the detection of linearly polarized gamma rays, the Compton scattering process is of interest to us. We require that the incident gamma rays can satisfy the condition that they first undergo Compton scattering in the converter and are finally stopped by the absorber. The typical effective Compton scattering process and the detection process of the polarimeter are described as follows. Generally, when a linearly polarized photon is incident in the polarimeter, the photon first undergoes Compton scattering in the converter. At this time, the information on the position of the scattering point and the energy of the recoil electron can be measured by the converter, while the recoil electron will be tracked if it creates a trail in the converter. Then the absorber absorbs the scattered photon and obtains the energy of the scattered photon and the position information of the absorption point. Of course, in addition to the above, there are also cases where recoil electrons pass through the converter and are absorbed by the absorber (see γ_2 in Fig. 7), as well as cases where scattered photons undergo multiple Compton scattering before being completely stopped by the absorber (see γ_2 in Fig. 7). It is clear from Fig. 7 that γ_1 and γ_2 are valid events that satisfy the condition. Finally, the simulation results can be obtained by analyzing these valid events.

A. Polarization response to monoenergetic photons

The fully linearly polarized (100%) and non-polarized (0%) homogeneous on-axis photon beams with an energy of 200 keV were used in the simulation experiments, where the other configuration parameters of both beams were identical (after here, photon beams are considered to be on-axis incidence if not otherwise specified). For a 100% linearly polarized photon beam, the polarization vector was (1, 0, 0). The raw azimuthal scatter angle distributions were obtained after the analysis of simulated data, as shown in Fig. 8. As can be seen in Fig. 8, the polarimeter has a significant response to polarized photons (see the blue curve) relative to unpolarized photons (see the black curve). It should be noted, however, that although the blue curve approximately obeys the cosine distribution, it is affected and distorted by the systematic modulation due to the non-uniformity of the detector,
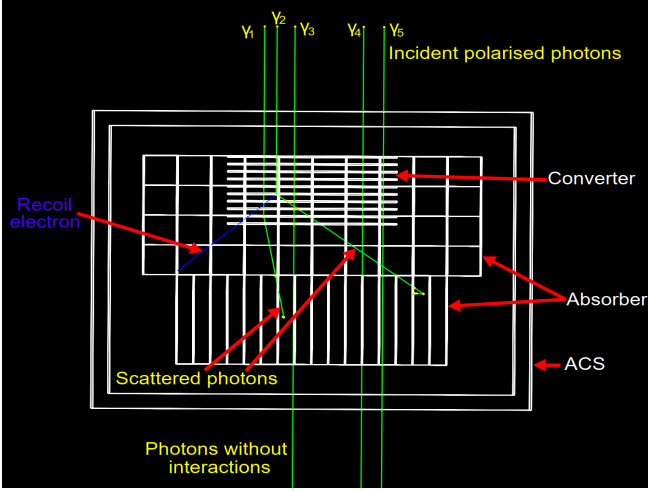
Fig. 7. (Color online) Interaction processes and traces left by gamma rays with an energy of 1000 keV incident on-axis into the polarimeter. Note: To make the trajectory of the particles in the polarimeter clearer, we have given a front view of the detector.
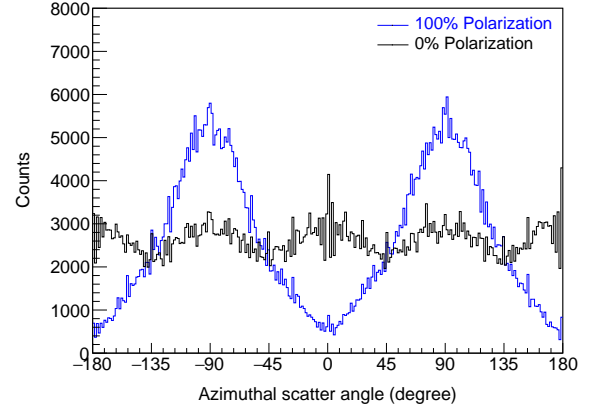

Fig. 8. (Color online) The raw azimuthal scatter angle distributions obtained from simulations that 100% (blue) and 0% (black) linearly polarized photon beams with an energy of 200 keV were on-axis incidence.
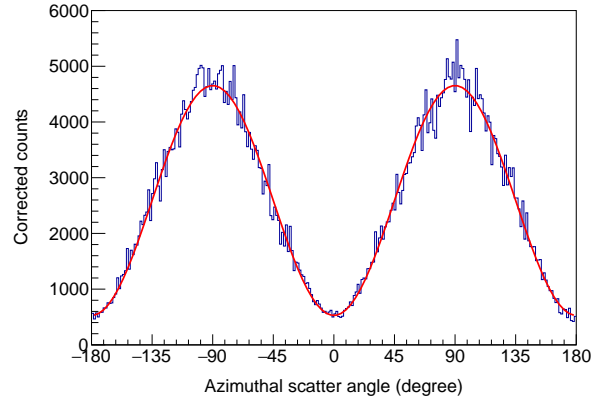
and it might be difficult to be fitted by Eq. (3). In addition, for the azimuthal angle distribution generated by unpolarized photons in the detector (see the black curve in Fig. 8), an apparent spurious modulation (the black curve is not perfectly uniformly distributed) is shown owing to the non-uniformity of the detector response along the azimuthal angle (i.e., the effect of the non-uniform response). Therefore, the raw azimuthal angle distribution needs to be corrected in order to eliminate the impact of this systematic modulation on the modulation curve. To obtain the corrected azimuthal angle distribution, we can follow the formula [2, 37]

$$f_{cor}(\varphi) = \frac{f(\varphi)}{f_{non}(\varphi)} \quad (7)$$

to correct the raw distribution. Here, $f(\varphi)$ is the raw azimuthal angle distribution generated by polarized photons (as the blue curve in Fig. 8), $f_{non}(\varphi)$ is the azimuthal angle distribution produced by unpolarized photons with the same energy and incident direction as the polarized photon (as the black curve in Fig. 8), and $f_{cor}(\varphi)$ is the corrected azimuthal angle distribution. Figure 9 illustrates the corrected modulation curve (after here, all modulation curves shown and analyzed are corrected). Compared with the raw modulation curve (see the blue curve in Fig. 8), the corrected modulation curve obeys the cosine distribution perfectly and can be well-fitted by Eq. (3) (see Fig. 9). The modulation factor μ_{100} can be calculated using the fitting parameters, which is 0.80±0.01. Also, 0.2°±0.2° is obtained to serve as the polarization direction of the incident photons, which is in good agreement with the actual direction (0°). From the above simulation results, it can be evident that the polarization response and performance of the polarimeter are excellent.

Figure 10 presents the corrected modulation curves fitted by Eq. (3) for four different polarization directions of the photon beam with an energy of 200 keV. The polarization parameters, such as polarization angle and modulation factor,

Fig. 9. (Color online) The azimuthal scatter angle distribution was obtained after the correction of the raw distribution (blue) in Fig. 8. The red curve was generated by fitting the corrected distribution by Eq. (3).

of the incident photons with four different polarization directions were obtained and listed in Table 2. From the simulation results in Table 2, it can be concluded that the polarimeter can precisely determine the polarization angle with an error of 0.2° no matter how the polarization direction of the incident photons is changed, and the obtained modulation factors are quite large and remain essentially constant.

During the data analysis, the Compton scattering events produced by polarized photons with an energy of 200 keV were selected with the Compton scattering angle as the filtering condition, and the dependence of the modulation factor on the Compton scattering angle can be obtained as shown in Fig. 11(a). As can be seen in Fig. 11(a), the modulation factor is smaller in the region of large and small scattering angles, yet it increases significantly in the region of medium scatter-
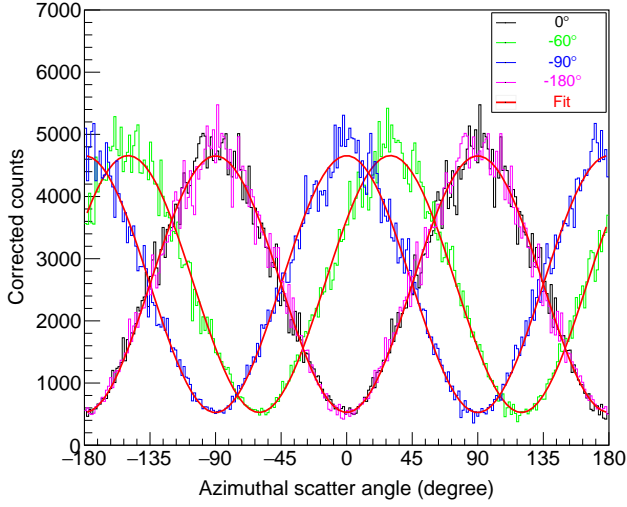
Fig. 10. (Color online) Corrected modulation curves and their best-fit curves (red). The polarization directions of the photon beams are 0° (black), -60° (green), -90° (blue), and -180° (magenta), respectively.

TABLE 2. Polarization parameters for polarized photons with polarization directions 0°, -60°, -90°, and -180°, respectively.

Polarization direction setup (degree)	Polarization angle simulated (degree)	Modulation factor μ_{100} simulated
0	0.2±0.2	0.80±0.01
-60	-60.2±0.2	0.80±0.01
-90	-90.2±0.2	0.80±0.01
-180	-179.8±0.2	0.80±0.01
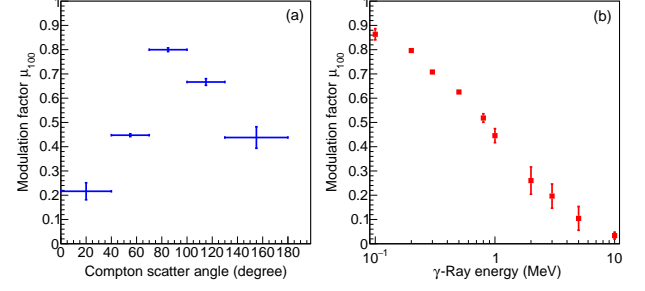
Fig. 11. (Color online) Dependence of the modulation factor on the Compton scattering angle (left panel, (a)) and the photon energy (right panel, (b)) for the monoenergetic photons.
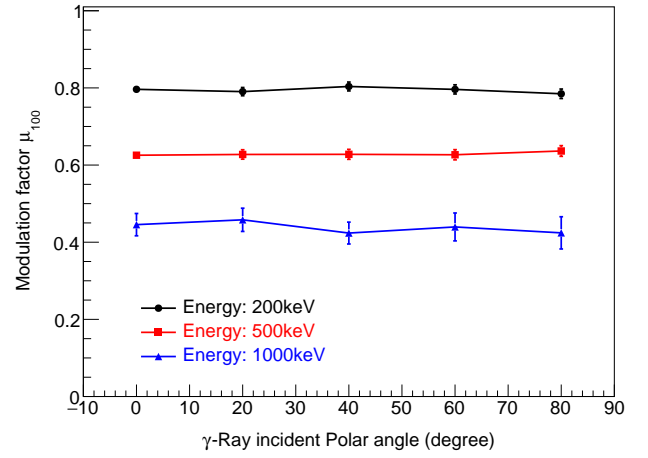
Fig. 12. (Color online) Dependence of the modulation factor on the incident polar angle for photons with energies of 200 keV, 500 keV, and 1000 keV.

ing angles. Figure 11(b) shows the relationship between the energy of the incident polarized photons (100 keV, 200 keV, 300 keV, 500 keV, 800 keV, 1000 keV, 2000 keV, 3000 keV, 5000 keV, and 10000 keV) and the modulation factor. It is apparent that the modulation factor decreases with the increase of the incident photon energy. From the simulation results in Fig. 11, we can conclude that the modulation of the azimuthal angle distribution is most significant at lower energies and medium Compton scattering angles, which is consistent with the theoretical results in Fig. 3.

Polarized photons with energies of 200 keV, 500 keV, and 1000 keV were simulated to be incident into the polarimeter at five different polar angles (0°, 20°, 40°, 60°, and 80°). Then three curves of the modulation factor versus incident polar angle were obtained, as shown in Fig. 12. The three relationship curves show that the modulation factor is almost unaffected by the off-axis incidence (not dependent on the incident polar angle of the photon), indicating that the polarimeter can still maintain a stable and remarkable polarization response to photons with different incidence angles. In addition, the results verify that such a polarimeter design has a large FoV.

B. Polarization response to a Crab-like source

Two Crab-like sources with a fully linearly polarized (100%) gamma-ray beam and an unpolarized (0%) gamma-ray beam (see Sec. II D for detailed parameters) were used in the simulation experiments of on-axis incidence on the polarimeter, provided that all other configurations were the same. The modulation factor was obtained by fitting the corrected modulation curve generated by 100% linearly polarized photons with Eq. (3), which had a value of 0.76±0.01. It can be observed that the polarimeter has a good response to continuous polarization photon spectra in addition to being sensitive to monoenergetic polarization photon spectra.

Since the polarization degree of the polarized photons emitted by the cosmic gamma-ray sources may not always be 100% but may be partially polarized, it is necessary to study the polarization response of the polarimeter to photons of different polarization degrees. The simulated modulation factor μ (see Eq. (4)) and the simulated polarization degree P (see Eq. (5)) were obtained by illuminating the polarimeter with photon beams emitted by the Crab-like sources with differ-

ent polarization degrees (1.0, 0.8, 0.6, 0.4, 0.2, and 0.1). The simulation results for the two polarization parameters mentioned above are presented in Table 3. From the data in the first and third columns in Table 3, it can be found that the modulation factor decreases as the polarization degree of the photon falls, which indicates that the sensitivity of the detector to photons with small polarization degree decreases, and this phenomenon is consistent with the theory. In addition, the data in the first and second columns in Table 3 show that the simulated polarization degrees are in good agreement with the actual set polarization degrees within the error tolerance. Therefore, we can assume that the polarimeter has a good ability to preserve the polarization degree of the incident photons or that the polarimeter can recover the incident photon polarization degree well.

TABLE 3. The simulated modulation factor μ (see Eq. (4)) and the simulated polarization degree P (see Eq. (5)) for the different polarization degrees of the incident photons from the Crab-like sources.

Crab-like source polarization degree setup	Polarization degree P simulated	Modulation factor μ simulated
1	1.00±0.02	0.76±0.01
0.8	0.80±0.02	0.61±0.01
0.6	0.59±0.02	0.45±0.01
0.4	0.39±0.01	0.30±0.01
0.2	0.20±0.01	0.15±0.01
0.1	0.09±0.01	0.07±0.01

The polarization sensitivity (MDP) can be defined as Eq. (6), a crucial performance parameter for a polarimeter, and characterizes the minimum polarization that a polarimeter can detect. The MDP of the polarimeter can be estimated by simulation. When the Crab-like source and background components were used for the simulation experiments of the polarimeter, the relationship curve between the MDP@3σ and the observation time was obtained, as shown in Fig. 13. It can be seen that the polarization detection capability of the polarimeter increases with observation time. During the twenty-four hours observation period, the MDP@3σ of the polarimeter is 8.2%. When the observation time reaches 10^6 seconds (~277.8 hours), the polarimeter is capable of detecting a 2.4% polarized Crab-like source. In conclusion, the polarimeter with excellent polarization detection capability can be well used to detect the polarization information of soft gamma rays in space to study various astronomical sources.

IV. SUMMARY

As a new astronomical tool, cosmic gamma-ray polarization can help explain various astrophysical phenomena and mechanisms from a unique dimension, yet it isn't easy to measure. Currently, there is no effective dedicated soft gamma-ray polarimeter operating in orbit. Small satellite technology is developing rapidly and has unique advantages compared to traditional large satellites. Given those mentioned above, developing a high-performance dedicated space
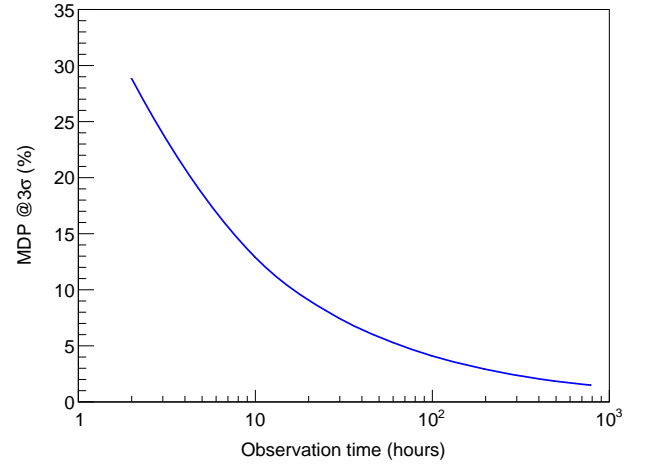

Fig. 13. (Color online) The polarization sensitivity (MDP) of the polarimeter for a Crab-like source as a function of the observation time.

soft gamma-ray polarimeter is necessary. The idea of using a constellation of multiple microsatellites to detect the polarization of gamma rays in space is promising. In this paper, we have studied one of the microsatellites in the constellation in detail. First, a novel structure was designed, which included a multilayer double-sided silicon strip converter in the upper part of the detector, a pixel-type CsI array absorber on five sides except the upper side of the converter, and a plastic scintillator ACS at the outermost side. Then, the mass model of the polarimeter was constructed and simulated in detail by setting the performance parameters of each sub-detector, the different gamma-ray polarization sources, and the background components using the dedicated simulation software based on the Monte Carlo method. For 100% polarized photons with an energy of 200 keV that were on-axis incidence, the polarimeter achieved a modulation factor of 0.80±0.01. The modulation factor of the polarimeter showed little dependence on the direction of incidence of the photons. In addition, the polarimeter could precisely measure the polarization angle of the incident photon at an accuracy of 0.2 degrees. For on-axis incident photons in the energy range of 0.1-10 MeV from a Crab-like polarization source, the polarization response of the polarimeter remained remarkable with a modulation factor of 0.76±0.01 (100% polarization), and the polarization degree of the incident photons could be accurately measured with a maximum error of 0.02. At the same time, the polarimeter exhibited excellent polarization sensitivity, and the MDP@3σ of the polarimeter could reach 2.4% at an exposure of 10^6 seconds. Undeniably, the outstanding performance demonstrated by the polarimeter also depends to some extent on its wide FoV (~2π sr) and potent background suppression. Additionally, the simulation results of the polarimeter that the polarization response of the polarimeter is most pronounced at lower energy and medium scattering angle were in good agreement with the theoretical law.

In summary, the idea of using microsatellites to detect soft

gamma-ray polarization proposed in this paper is promising and can bring new thoughts for future space exploration. Additionally, the polarimeter of the novel configuration designed in this paper has shown excellent polarization detection capability after being verified by simulation experiments, which has great potential to be competent for the future task of soft gamma-ray polarization detection in space. In this paper, the configuration design, simulation methods, and simulation results of the polarimeter will lay a solid foundation for the development of the future polarization detection satellite prototype, will strongly promote the smooth development of possible future constellation programs, and will provide a valuable reference for the design of other polarization detectors in the future.

[1] R. Mignani, A. Shearer, A. Slowikowska et al., *Astronomical Polarisation from the Infrared to Gamma Rays*, (Springer, Switzerland Cham, 2019), pp. 109—111.

[2] S. Komura, A. Takada, Y. Mizumura et al., Imaging Polarimeter for a Sub-MeV Gamma-Ray All-sky Survey Using an Electron-tracking Compton Camera. Astrophys. J. **839**, 41 (2017). doi: 10.3847/1538-4357/aa68dc

[3] K. Toma, T. Sakamoto, B. Zhang et al., Statistical Properties of Gamma-Ray Burst Polarization. Astrophys. J. **698**, 1042—1053 (2009). doi: 10.1088/0004-637X/698/2/1042

[4] V. Tatischeff, A.D. Angelis, C. Gouiffès et al., e-ASTROGAM mission: a major step forward for gamma-ray polarimetry. J. Astron. Telesc. Inst. **4**, 011003 (2017). doi: 10.1117/1.JATIS.4.1.011003

[5] N. Produit, F. Barao, S. Deluit et al., POLAR, a compact detector for Gamma Ray Bursts photon polarization measurements. Nucl. Instrum. Methods Phys. Res. Sect. A **550**, 616—625 (2005). doi: 10.1016/j.nima.2005.05.066

[6] Y.Z. Fan, Interpretation and implications of the non-detection of GeV spectrum excess by the Fermi Gamma-ray Space Telescope in most gamma-ray bursts. Mon. Not. R. Astron. Soc. **397**, 1539—1548 (2009). doi: 10.1111/j.1365-2966.2009.15018.x

[7] A.D. Angelis, V. Tatischeff, I.A. Grenier et al., Science with e-ASTROGAM: A space mission for MeV–GeV gamma-ray astrophysics. J. High Energy Astrop. **19**, 1—106 (2018). doi: 10.1016/j.jheap.2018.07.001

[8] J.D. Schnittman, J.H. Krolik, X-ray Polarization from Accreting Black Holes: Coronal Emission. Astrophys. J. **712**, 908—924 (2010). doi: 10.1088/0004-637X/712/2/908

[9] F. Lei, A.J. Dean, G.L. Hills, Compton Polarimetry in Gamma-Ray Astronomy. Space Sci. Rev. **82**, 309—388 (1997). doi: 10.1023/A:1005027107614

[10] H.C. Zhang, C. Diltz, M. Böttcher, Radiation and Polarization Signatures of 3D Multi-zone Time-dependent Hadronic Blazar Model. Astrophys. J. **829**, 69 (2016). doi: 10.3847/0004-637X/829/2/69

[11] M. Böttcher, Progress in Multi-Wavelength and Multi-Messenger Observations of Blazars and Theoretical Challenges. Galaxies **7**, 20 (2019). doi: 10.3390/galaxies7010020

[12] P. Laurent, J. Rodriguez, J. Wilms et al., Polarized Gamma-Ray Emission from the Galactic Black Hole Cygnus X-1. Science **332**, 438—439 (2011). doi: 10.1126/science.1200848

[13] H. Krawczynski, A. Garson, Q. Guo et al., Scientific prospects for hard X-ray polarimetry. Astropart. Phys. **34**, 550—567 (2011). doi: 10.1016/j.astropartphys.2010.12.001

[14] M.C. Weisskopf, E.H. Silver, H.L. Kestenbaum et al., A precision measurement of the X-ray polarization of the Crab Nebula without pulsar contamination. Astrophys. J. **220**, L117—L121 (1978). doi: 10.1086/182648

[15] M.L. McConnell, J.M. Ryan, D.M. Smith et al., RHESSI as a Hard X-Ray Polarimeter. Sol. Phys. **210**, 125—142 (2002). doi: 10.1023/A:1022413708738

[16] M. Forot, P. Laurent, I. Grenier et al., Polarization of the Crab Pulsar and Nebula as Observed by the INTEGRAL/IBIS Telescope. Astrophys. J. Lett. **688**, L29—L32 (2008). doi: 10.1086/593974

[17] D. Yonetoku, T. Murakami, S. Gunji, et al., DETECTION OF GAMMA-RAY POLARIZATION IN PROMPT EMISSION OF GRB 100826A. Astrophys. J. Lett. **743**, L30 (2011). doi: 10.1088/2041-8205/743/2/L30

[18] H.L. Xiao, Y.W. Dong, B.B. Wu et al., POLAR Gamma Ray Burst Polarimeter onboard TG-2 Spacelab. Manned Spaceflight **21**, 32—36+43 (2015). (in Chinese) doi: 10.3969/j.issn.1674-5825.2015.01.006

[19] V. Bhalerao, D. Bhattacharya, A. Vibhute et al., The Cadmium Zinc Telluride Imager on AstroSat. J. Astrophys. Astron. **38**, 31 (2017). doi: 10.1007/s12036-017-9447-8

[20] Y. Kishimoto, S. Gunji, Y. Ishigaki et al., Basic Performance of PHENEX: A Polarimeter for High ENErgy X rays. IEEE T. NUCL. SCI. **54**, 561–566 (2007). doi: 10.1109/TNS.2007.897827

[21] S. Larsson, M. Pearce, PoGO : The polarised gamma-ray observer. Nucl. Instrum. Methods Phys. Res. Sect. A **525**, 148–152 (2004). doi: 10.1016/j.nima.2004.03.036

[22] M. Friis, M. Kiss, V. Mikhalev et al., The PoGO+ Balloon-Borne Hard X-ray Polarimetry Mission. Galaxies **6**, 30 (2018). doi: 10.3390/galaxies6010030

[23] P.F. Bloser, J.S. Legere, J.R. Macri et al., GRAPE - A Balloon-Borne Gamma-Ray Polarimeter Experiment. Chin. J. Astron. Astrophys. **6**, 393—397 (2006). doi: 10.48550/arXiv.astro-ph/0508314

[24] T. Satoru, A. Shigeki, K. Keiki et al., GRAINE project: The first balloon-borne, emulsion gamma-ray telescope experiment. Prog. Theor. Exp. Phys. **2015**, 43H01 (2015). doi: 10.1093/ptep/ptv046

[25] P.F. Bloser, J.M. Ryan, M.L. McConnell et al., The MEGA project: Science goals and hardware development. New Astron. Rev. **50**, 619–623 (2006). doi: 10.1016/j.newar.2006.06.001

[26] J.-L. Chiu, S.E. Boggs, H.-K. Chang et al., The upcoming balloon campaign of the Compton Spectrometer and Imager (COSI). Nucl. Instrum. Methods Phys. Res. Sect. A **784**, 359–363 (2015). doi: 10.1016/j.nima.2014.11.099

[27] X. Wen, X.W. Zhang, Analysis of current developments in the field of modern small satellites. Journal of Shenyang Aerospace University **30**, 33–36+46 (2013). (in Chinese) doi: 10.3969/j.issn.2095-1248.2013.05.007

[28] Z.G. Bai, Development Achievements and Prospects of China Modern Small Satellite. Spacecraft Engineering **28**, 1–8 (2019). (in Chinese) doi: 10.3969/j.issn.1673-8748.2019.02.001

[29] J.X. Wen, X.T. Zheng, J.D. Yu et al., Compact CubeSat Gamma-ray detector for GRID mission. Nucl. Sci. Tech. **32**,

107–117 (2021). doi: 10.1007/S41365-021-00937-4

[30] O. Engvold, J.-C. Vial, A. Skumanich, *The Sun as a Guide to Stellar Physics* , (Elsevier, Amsterdam, 2019), pp. 189.

[31] W.F. Liu, X.M. Liu, S.W. Tang et al., Study of the detection unit of the calorimeter for the next generation Compton telescope. Nuclear Techniques **43**, 20–28 (2020). (in Chinese) doi: 10.11889/j.0253-3219.2020.hjs.43.010203

[32] V. Bindi, A.D. Guerra, G. Levi et al., Preliminary study of silicon photomultipliers for space missions. Methods Phys. Res. Sect. A **572**, 662–667 (2007). doi: 10.1016/j.nima.2006.12.011

[33] X.M. Liu, S.W. Tang, W.F. Liu et al., Study of the γ -Ray Detector of Dual-ended Readout Based on SiPM. Nuclear Physics Review **37**, 757–764 (2020). (in Chinese) doi: 10.11804/NuclPhysRev.37.2019CNPC03

[34] A. Zoglauer, R. Andritschke, F. Schopper, MEGAlib – The Medium Energy Gamma-ray Astronomy Library. New Astron. Rev. **50**, 629—632 (2006). doi: 10.1016/j.newar.2006.06.049

[35] R. Brun, F. Rademakers, ROOT — An object oriented data analysis framework. Nucl. Instrum. Methods Phys. Res. Sect. A **389**, 81—86 (1997). doi: 10.1016/S0168-9002(97)00048-X

[36] S. Agostinelli, J. Allison, K. Amako et al., Geant4—a simulation toolkit. Nucl. Instrum. Methods Phys. Res. Sect. A **506**, 250–303 (2003). doi: 10.1016/S0168-9002(03)01368-8

[37] A.C. Zoglauer, *First Light for the Next Generation of Compton and Pair Telescopes*. Dissertation for the Doctoral Degree (Technical University of Munich, Munich, 2005), pp. 41—125.

[38] R. Rando, The all-sky medium energy gamma-ray observatory. J. Instrum. **12**, C11024 (2017). doi: 10.1088/1748-0221/12/11/C11024

[39] V. Schönfelder, The imaging gamma-ray telescope COMP-TEL aboard GRO. Adv. Space Res. **11**, 313–322 (1991). doi: 10.1016/0273-1177(91)90183-K

[40] S.E. Boggs, The Advanced Compton Telescope mission. New Astron. Rev. **50**, 604–607 (2006) doi: 10.1016/j.newar.2006.06.076

[41] K. Kamiya, *Compton Recoil Electron Tracking With the TIGRE Gamma-Ray Balloon Experiment*. Dissertation for the Doctoral Degree (University of California, Riverside, Riverside, 2011), pp. 53—61.

[42] M. Galloway, A. Zoglauer, S.E. Boggs et al., A combined Compton and coded-aperture telescope for medium-energy gamma-ray astrophysics. A&A **614**, A93 (2018) doi: 10.1051/0004-6361/201731122

[43] A. Zoglauer, S.E. Boggs, M. Galloway et al., Design, implementation, and optimization of MEGAlib's image reconstruction tool Mimrec. A&A **652**, 568–571 (2011) doi: 10.1016/j.nima.2010.08.043

[44] P. Cumani, M. Hernanz, J. Kiener et al., Background for a gamma-ray satellite on a low-Earth orbit. Exp. Astron. **47**, 273–302 (2019). doi: 10.1007/s10686-019-09624-0

[45] A. Akyüz, D. Bhattacharya, D.D. Dixon et al., Polarization measurements with an imaging gamma-ray telescope. Exp. Astron. **6**, 275—284 (1995). doi: 10.1007/BF00418325

[46] R. Campana, M. Orlandini, E.D. Monte et al., The radiation environment in a low earth orbit:the case of BeppoSAX. Exp. Astron. **37**, 599–613 (2014). doi: 10.1007/s10686-014-9394-1

[47] M. Tavani, G. Barbiellini, A. Argan et al., The AGILE mission. Astron. Astrophys. **502**, 995—1013 (2009). doi: 10.1051/0004-6361/200810527